The Astrophysical Journal, 876:154 (16pp), 2019 May 10 https://doi.org/10.3847/1538-4357/ab16d6

Interactions between Radio Galaxies and Cluster Shocks. I. Jet Axes Aligned with Shock Normals

Chris Nolting[1], T. W. Jones[1], Brian J. O'Neill[1], and P. J. Mendygral[2]
[1] School of Physics and Astronomy, University of Minnesota, Minneapolis, MN, USA
[2] Cray Inc., Bloomington, MN, USA
Received 2019 February 22; revised 2019 April 4; accepted 2019 April 5; published 2019 May 15

Abstract

We report from a study utilizing 3D MHD simulations, including cosmic-ray electrons, of the interactions between radio galaxies (RGs) and dynamically active intracluster media (ICMs). Here we consider interactions involving plane ICM shocks having Mach numbers 2–4 and their normals aligned with steady, active bipolar RG jets penetrating uniform, stationary ICMs. The shock impact disrupts the preformed RG jet cocoons into ring vortex structures. Sufficiently strong post-shock winds can stop and even reverse the upwind jet and strip jets to virtually naked states, leaving them without a surrounding cocoon. Strong shock-induced vorticity can also disrupt the downwind jet, so that the ring vortex remnant of the cocoons appears ahead of that jet's visible terminus. Magnetic field amplification in the ring vortex can significantly enhance its synchrotron emissions well after the vortex becomes isolated from the RG and its fresh cosmic-ray electron supply. We examine these dynamics and their observable consequences in detail.

Key words: galaxies: clusters: intracluster medium – galaxies: jets – magnetohydrodynamics (MHD) – methods: numerical – radio continuum: galaxies – shock waves

1. Introduction

Galaxy clusters form by way of accretion and occasional mergers. Those behaviors are inherently nonsymmetrical and unsteady, which drives strong motions in the diffuse intracluster media (ICMs). Additional ICM "stirring" comes, for example, by way of gravitational interactions with nearby halos, galactic winds, and jets. Consequently, ICMs should be dynamic, not static, environments. Cluster dynamics include turbulence, sloshing motions, infall flows, and shocks (e.g., Markevitch et al. 2002; Tittley & Henriksen 2005; Voit 2005; Brunetti et al. 2008; Schekochihin et al. 2009; Brüggen et al. 2012; ZuHone & Roediger 2016). Proper characterization of an ICM's dynamical state can reveal much about the cluster's recent history (e.g., Nagai et al. 2007; Kravtsov & Borgani 2012; Walker et al. 2019). On the other hand, ICM motions are quite challenging to measure directly with current instruments.[3] Some moderately strong ICM shocks with shock normals close to the plane of the sky have been detected in the X-ray band in relatively high-density regions (e.g., Markevitch et al. 2002; van Weeren et al. 2016). Diffuse, nonthermal radio emissions from locally reaccelerated relativistic cosmic-ray electrons (CRe) within ICMs also evidently reveal large-scale dynamical structures including shocks and, probably, turbulence (e.g., van Weeren et al. 2019). These features are currently the most widely applied signatures of ICM dynamics.

At the same time, radio galaxies (RGs) with nonthermal structures extending tens to hundreds of kpc from their active galactic nucleus (AGN) of origin are common throughout cluster volumes, including regions where X-ray emissions are faint (e.g., Padovani 2016; Garon et al. 2019). The properties of these RGs are very sensitive to the details of the interactions with the ambient ICM. Beyond their source galaxies, RGs are visible largely because of their interactions with ICMs. Because of these interactions, it is important to learn how to use RG properties as "ICM weather vanes," i.e., to use RG properties on scales of tens of kpc and beyond to extract insights about the associated ICM dynamics.

Relative RG–ICM motions and their variations can be particularly telling, since they strongly modify the symmetry of an RG from that provided by the host AGN. Jet bending due to relative motion between the host galaxy and the ICM has been accepted for several decades as the principal cause of the formation of so-called "head–tail" RGs (Begelman et al. 1979; Jones & Owen 1979). Of course, the existence of a head–tail structure by itself reveals only the presence of relative motion, not the motion of either constituent relative to the cluster center. Other details are necessary to establish the full dynamical picture. In this, we should be mindful that because both galaxy motions and bulk ICM motions derive from the same gravitational potential, they can be similar in magnitude. However, galaxy motions are "particle-like," while ICMs behave as fluids on these scales.

In recognition of the presence of large-scale ICM shocks during merger events, it was pointed out some time ago that the impact of an ICM shock on an RG-formed ICM cavity can transform the cavity into a "doughnut-like" ring vortex, while potentially brightening its synchrotron emissions by way of compression and magnetic field amplification (see, e.g., Enßlin & Brüggen 2002 and Pfrommer & Jones 2011 for simulation results and possible observed examples). This topological transformation results from shear induced by the abruptly increased shock speed (and subsequent post-shock flow speed) inside the low-density cavity (Enßlin & Brüggen 2002). The same physics has been studied in detail in a laboratory environment using helium bubbles being shocked by air to create vortex rings (e.g., Ranjan et al. 2008). In this work and a companion paper, we deal with the consequences of the scenario in which a shock interacts with the lobes of an RG that contains active jets initially penetrating a stationary medium.

[3] The most precise measurements currently available are from Hitomi Collaboration et al. (2016), which measured a velocity dispersion of $164 \pm 10\ \mathrm{km\ s^{-1}}$ near the core of the Perseus cluster utilizing the Hitomi SXS instrument.

The shock passage through the low-density lobes of such an RG does lead to formation of vortex rings (that may eventually merge into a single ring). However, the presence of active jets adds considerable richness to the evolution of the impacted RG. Our goals are to understand the underlying physics that controls this evolution and to look for observable dynamical signatures.

There are a growing number of clusters containing "highly deformed" RGs whose properties and/or juxtaposition with an X-ray shock might suggest a physical RG–shock encounter (e.g., Mandal et al. 2019; Wilber et al. 2019). In some cases, the RG morphology and positional relation to the shock suggest that the pre-shock RG had a head–tail structure (e.g., Bonafede et al. 2014; Shimwell et al. 2014; van Weeren et al. 2017; Mandal et al. 2019). These shock–radio tail encounters could be useful diagnostics once their evolution is understood and may be relatively easy to spot. However, prior to shock impact, RG tails are complex and heterogeneous structures, which substantially alters and complicates subsequent shock interactions compared to interactions with RG lobes, including those with enclosed jets. We will examine the shocked tail problem in a separate paper in preparation (B. J. O'Neill et al. 2019b, in preparation). We focus first on shock collisions with straight, active, lobed RGs. Active RG jets add significantly to the full evolutionary story, and the character of the jet influence depends on the orientation between the shock normal and the RG jet axis. Fortunately, much of the range in variation can be captured by examining the simple limits in which the jets are either aligned with the impacting shock normal or orthogonal to the shock normal. In this paper, we focus on the aligned jet–shock normal case, making reference as needed to consequences when the ideal symmetry is broken. In a companion paper to this one (C. Nolting et al. 2019, in preparation), we conduct an analogous examination of the orthogonal impact case. An additional, complementary paper (B. J. O'Neill et al. 2019a, in preparation) examines in detail the evolution and emissions from AGN jets forming within steady winds, i.e., head–tail formation, including basic dependencies on wind–jet orientation.

Jones et al. (2017) emphasized from analytic arguments that one distinctive result of an aligned RG–shock impact is a decreased rate of extension of the forward (upstream) RG jet compared to the extension rate of the downstream jet. For sufficiently strong shocks, they suggested that the upstream jet might actually be reversed, leading to essentially one-sided "head–tail" RG morphologies. At least one single-tail RG has been been identified in a merging cluster that could be a candidate for an aligned shock–RG encounter. Specifically, "source C" in the merging cluster A2256 (e.g., Rottgering et al. 1994; Owen et al. 2014) exhibits a narrow (width $\sim$1 kpc, even $\gtrsim$100 kpc projected distance from the AGN), remarkably straight tail extending for a projected distance $\sim$1 Mpc to the NW of the AGN, with no evident kiloparsec-scale structure on the opposite side of the host. The considerable projected length of this tail makes relativistic beaming an unlikely explanation for the asymmetry (Terni de Gregory et al. 2017), while the large projected length combined with the very narrow width over the large projected distance significantly reduces the odds that it is simply a typical twin-tail RG viewed close to the plane of the two tails (but see Section 4.3 for more on this issue). We shall see below that, in fact, some basic properties similar to those of source C may be natural outcomes from an aligned RG–shock encounter followed by immersion of the surviving jet in a strong, aligned, post-shock wind. Our purpose here is to explore this basic scenario, not to model that specific object. Our analysis examines the underlying shock–RG dynamics, including evolution of magnetic fields and CRe from the source AGN, as well as associated radio synchrotron emissions in simulations motivated by this example.

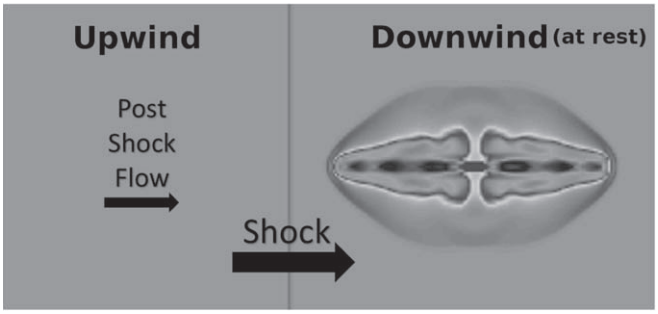

Figure 1. Basic geometry of modeled aligned shock–RG encounters.

The remainder of the paper is organized as follows. Section 2 outlines the physical scenario in terms of shock–lobe (Section 2.1) and wind–jet (Section 2.2) interactions. Section 3 describes our simulation specifics, including numerical methods (Section 3.1) and details of our simulation setups (Section 3.2). In Section 4 we discuss the results of the simulations, while Section 5 provides a brief summary of results.

2. Outline of Aligned Shock–RG Interaction Dynamics

The analytic basics of an aligned shock–RG encounter can be outlined rather simply. Our brief discussion largely follows Jones et al. (2017). Readers are referred to that work and references therein for further details. Figure 1 illustrates the basic scenario we are addressing in this paper. Although our outline in this section deals strictly with aligned jet–shock encounters, our simulations verify that many aspects of modestly misaligned encounters, aside from obvious symmetry issues, are very similar. Specifically, the treatments of shock propagation through lobes (Section 2.1) and jet terminus advancement within a headwind or tailwind (Section 2.2) applying momentum flux in the aligned wind velocity component remain quite useful in understanding misaligned shock–RG encounters.

In the following analysis, all velocities are referenced to the rest frame of the RG-source AGN. We define "upwind" to point in the direction the shock is coming from, while "downwind" points in the direction the shock is going. Thus, the upwind components of the RG encounter the shock before the downwind components (see Figure 1). In this paper, the AGN itself is assumed to be at rest with respect to the unshocked ICM (see B. J. O'Neill et al. 2019a, in preparation, for alternative choices). For notation clarity, we mention that, henceforth, subscripts "*j*" and "*s*" refer to the jet and the shock, while subscripts "*i*" and "*w*" point to the unmodified ICM and the post-shock wind. When combined, as "*ji*" or "*jw*," for example, the notation points to jet properties in the ICM or jet properties in the wind.

Since much of the physics of shock–RG interactions depends on the ICM post-shock pressure, flow velocity, and sound speed, we list up front results from the standard Rankine–Hugoniot relations (using $\gamma = 5/3$) connecting the shock Mach

number in the ICM, $M_{si} = |v_{si}|/a_i$, and downstream pre-shock ICM conditions, P_i and $a_i = \sqrt{\gamma P_i/\rho_i}$, to the post-shock "wind" pressure, P_w; velocity, $|v_w|$; and sound speed, a_w. It is often convenient to utilize flow Mach numbers, so we also include the wind Mach number measured with respect to the post-shock pressure and density, $|M_w| = |v_w|/a_w$ (see Equation (5)). Below, we treat v_w as a signed velocity component, with $v_w > 0$ corresponding to a headwind as seen by a jet of interest. We have

$$\rho_w = \frac{4\mathcal{M}_i^2}{\mathcal{M}_i^2 + 3}\rho_i, \tag{1}$$

$$P_w = \frac{5M_{si}^2 - 1}{4}P_i, \tag{2}$$

$$|v_w| = \frac{3}{4}\frac{M_{si}^2 - 1}{M_{si}}a_i, \tag{3}$$

$$a_w = \frac{\sqrt{(M_{si}^2 + 3)(5M_{si}^2 - 1)}}{4M_{si}}a_i, \tag{4}$$

$$|M_w| = \frac{|v_w|}{a_w} = 3\frac{M_{si}^2 - 1}{\sqrt{(M_{si}^2 + 3)(5M_{si}^2 - 1)}}. \tag{5}$$

For the shocks of interest in this study, $2 \leqslant M_{si} \leqslant 4$, the post-shock conditions span $2.29 \leqslant \rho_w/\rho_i \leqslant 3.37$, $4.75 \leqslant (P_w/P_i) \leqslant 19.75, 1.13 \leqslant |v_w|/a_i \leqslant 7.13$, $1.44 \leqslant a_w/a_i \leqslant 1.94$, and $0.23 \leqslant |M_w| \leqslant 1.16$.

2.1. Shock–Lobe Collisions

Interactions between an ICM shock and a classical, lobed RG can be roughly decomposed into the impulsive impact of the shock discontinuity with its resultant aftermath and the subsequent, longer-term interactions with a post-shock wind flow. The principal modifications to a lobed RG from the shock impact itself come as the shock enters the very low density lobes (i.e., cocoons or cavities). The very low densities of the cavities ($\rho_c \ll \rho_i$, where subscript c is for cavity) are a direct consequence of their formation by fast, light jets. On the other hand, RG lobes should be in at least rough pressure balance with the unshocked ICM[4] ($P_c \sim P_i$). For our needs here, only approximate pressure balance matters, and we can similarly ignore any differences in lobe and ICM equations of state. Then, the sound speed in the lobe (cavity), $a_c \sim \sqrt{\rho_i/\rho_c}\, a_i \gg a_i$, where a_i is the sound speed in the unshocked ICM. As the shock enters a low-density lobe, the shock velocity increases (so $v_{sc} > a_c > v_{si} = M_{si}\, a_i$), although, because the lobe plasma is much hotter than the ICM, the internal shock Mach number, $M_{sc} = v_{sc}/a_c$, can be substantially less than the ICM shock Mach number, M_{si}; i.e., $M_{sc} < M_{si}$. For $\rho_c \lesssim 10^{-2}\rho_i$ and $M_{si} \sim 2$–4, relevant to our simulations described below, analytic results in Pfrommer & Jones (2011) suggest typical expected cavity shock velocities, $v_{sc} \sim 3$–$5\, v_{si}$, with cavity shock Mach numbers only slightly more than 1.

The shock penetrating the cavity pulls with it dense, post-shock ICM at a speed intermediate between the external and internal shock velocities. For conditions similar to those in the simulations reported here, Pfrommer & Jones (2011) found a propagation rate for the contact discontinuity (CD) separating the shocked ICM and the lobe plasma of $v_{\rm CD} \sim 1.2$–$1.4\, v_{si}$. Most importantly, the dense ICM inside the original cavity then runs ahead of the surrounding external shock. That generates strong shear along the original boundary between the lobe and the ICM with faster, forward flow inside and the effective return flow around the outside. Since the cross section of the original lobe boundary as seen from the shock plane was roughly circular, the outcome is a toroidal vortex ring tracing that boundary with its axis aligned to the shock normal (see, e.g., Figures 5 and 6).

Our simulations reported below reveal that the hot, low-density plasma originally inside the lobes becomes wrapped toward the inside of the vortex torus, surrounded by denser, cooler ICM material that carries most of the kinetic energy in the vortex. Typical for vortex flows, the gas pressure is largest on the outer perimeter, being enhanced in this situation by $\sim\rho_i v_{\rm CD}^2 > M_{si}^2\rho_i a_i^2$ over the post-shock wind pressure, P_w. For the vortex structures generated by $M_{si} \sim 2$–4 shocks, this pressure enhancement can easily exceed P_i by more than an order of magnitude. For the geometries of interest in this paper, the circulation around the vortex converges just upwind of where the vortex surrounds the axis of the downwind jet (so slightly closer to the AGN). As we will show, for stronger shocks, this can pinch or otherwise disrupt propagation of that jet. This converging flow also leads during this development to significant density enhancement in the post-shock ICM behind the vortex.

2.2. Jet Propagation in a Headwind or Tailwind

The AGN jets themselves primarily respond to conditions in the post-shock flow or wind. For aligned shock–jet encounters in particular, once in the post-shock ICM, the upwind jet finds itself in a high-density, high-pressure headwind. The downwind jet, if overrun by the ICM shock, will be embedded in a high-density, high-pressure tailwind. Since the jet facing upwind into the shock inevitably finds itself in a headwind, we concentrate on that situation, although we lay out the formalism so it applies to either a headwind or a tailwind. In either upwind or downwind situations, except for parameters tuned to match post-shock conditions, the dynamics also apply to more general situations in which an AGN simply finds itself embedded in a wind due to relative AGN–ICM motion. So, with an appropriate parameter adjustment, the jet behaviors outlined do not require a shock impact.

The simplest 1D model for jet terminus (or "head") propagation depends only on momentum flux balance at the jet terminus. Then, the adjustment in the advance rate of the terminus for a headwind or tailwind differs only by a sign in the effective momentum flux for the wind. To compute the propagation velocity of a jet "head," v_h, we first need the jet thrust, or total jet momentum flux. The fully relativistic momentum flux density of the jet, T_{mj}, can be written as $T_{mj} = w_j U_j^2/c^2 + P_j$, where $w_j = e_j + P_j$ is the enthalpy density in the jet, e_j is the energy density including rest-mass energy, P_j is the jet pressure, and $U_j = \Gamma_j v_j$ is the jet 4 velocity, with Γ_j being the jet Lorentz factor. In the nonrelativistic limit that applies to our simulations, $\Gamma_j \to 1$ and $w_j \to \rho_j c^2 + P_j \approx \rho_j c^2$. Then, the jet sound speed is defined as $a_j = c\sqrt{\partial P_j/\partial e_j} \xrightarrow{n.r.} \sqrt{\gamma P_j/\rho_j}$, where the final form is the nonrelativistic limit. The jet internal Mach number is

[4] In the simulations reported here, $\rho_c \lesssim 10^{-2}\ \rho_i$, with cavity pressure, $P_c \sim P_i$, before ICM shock impact.

$M_j = \Gamma_j v_j/(\Gamma_{s,j} a_j)$, with $\Gamma_{s,j} = 1/\sqrt{1-(a_j/c)^2}$, so that the total thrust of the jet, $T_{mj}A_j$, can be written as

$$T_{mj}A_j = \left(w_j \frac{U_j^2}{c^2} + P_j\right)A_j = (\gamma' M_j^2 + 1)P_j A_j, \quad (6)$$

$$\overrightarrow{s.s.}\ \gamma' M_j^2 P_j A_j, \quad (7)$$

where A_j is the jet cross-sectional area and $\gamma' = (\Gamma_{s,j}^2 a_j^2 w_j)/(P_j c^2)$. Here $\gamma' \to 2$ for an ideal relativistic equation of state, while $\gamma' \overrightarrow{n.r.}\ \gamma = \frac{5}{3}$ for an ideal monatomic nonrelativistic gas. The form in Equation (7) applies when the jet is supersonic. If the jet is supersonic, while both the velocity and equation of state are nonrelativistic, $T_{mj}A_j \approx \gamma M_j^2 P_j A_j = v_j^2 \rho_j A_j$. Although it is common and correct to use $v_j^2 \rho_j A_j$ to express jet thrust under these circumstances, we prefer in our analysis to use the equivalent $\gamma' M_j^2 P_j A \to \gamma M_j^2 P_j A_j$, since for pressure-confined jets, the local mean jet pressure, P_j, should adjust to become comparable to the pressure in the jet surroundings. This form keeps that issue visible. In our simulations, the jets are pressure-confined, and we find that P_j always adjusts approximately to the surroundings. We note for reference below that if we keep the jet thrust, $T_{mj}A_j$, fixed, then $M_j \propto 1/\sqrt{P_j}$ if the jet is supersonic. So, as a supersonic jet propagates from the unshocked ICM into the post-shock wind, the jet Mach number will decrease accordingly. A benefit of tracking the adjusted Mach number is maintaining awareness of whether or not the jet is supersonic at a location of interest.

Our immediate objective is to estimate the propagation velocity of the jet head, v_h, with respect to the AGN in the presence of a wind. If the jet head is propagating in an aligned wind of velocity v_w, density ρ_w, and pressure P_w, the total external momentum flux density on the "nose" of the jet is

$$(v_h + v_w)^2 \rho_w + P_w = [\gamma (M_h + M_w)^2) + 1]P_w, \quad (8)$$

where $v_w > 0$ corresponds to a headwind, while $v_w < 0$ represents a tailwind. In the second form, we set $M_h = v_h/a_w$ and $M_w = v_w/a_w$, with $a_w = \sqrt{\gamma P_w/\rho_w}$. Again, $M_w > 0$ refers to a headwind, while $M_w < 0$ is a tailwind. We can estimate v_h or M_h simply by assuming that the thrust of the jet in Equation (6) is matched by the external momentum flux distributed over an effective "head area," A_h, to be estimated empirically in comparison to A_j from the simulation results relation to Equation (10) below. The momentum balance relation becomes

$$(\gamma' M_j^2 + 1)\, P_j A_j = [\gamma (M_h + M_w)^2) + 1]P_w A_h. \quad (9)$$

Equation (9) can be solved for M_h to give

$$M_{hw} = \frac{v_h}{a_w} \approx -M_w + M_j \sqrt{\frac{\gamma' P_j A_j}{\gamma P_w A_h} + \frac{1}{\gamma M_j^2}\frac{P_j A_j - P_w A_h}{P_w A_h}}$$

$$\overrightarrow{n.r.,s.s.}\ -M_w + M_j \sqrt{\frac{A_j}{A_h}}, \quad (10)$$

where the last line provides the limiting nonrelativistic, supersonic form, assuming $P_j = P_w$, while dropping the term $(A_j - A_h)/(\gamma M_j^2 A_h)$ inside the square root We should keep in mind that M_j refers to the "local" internal Mach number of the jet before its terminal shock. With properly chosen parameters, Equation (10) would apply for advancement in any roughly aligned headwind or tailwind. In the absence of a wind, the AGN evolves in a stationary ICM with pressure, P_i, and sound speed, a_i, and we can express the undisturbed head advance Mach number as $M_h = v_h/a_i \approx M_{ji}\sqrt{A_j/A_h}$.

Since our focus here is primarily propagation in a post-shock wind, we have, assuming $P_j \sim P_w$,

$$M_{hw} \approx -M_w + M_{ji}\sqrt{\frac{P_i A_j}{P_w A_h}}, \quad (11)$$

with M_{ji} corresponding to the jet internal Mach number prior to its penetration into the post-shock region. From Equation (11), we can estimate that in a sufficiently strong headwind, the advance of the head reverses, so that the wind drives the jet head back toward its source. In that case, there is eventually only a downwind jet; that is, the RG effectively becomes a one-sided jet. Specifically, Equation (11) predicts that result for $M_w > M_{wc}$, with

$$M_{wc} = M_{ji}\sqrt{\frac{P_i A_j}{P_w A_h}}. \quad (12)$$

This dynamics applies only where the jets are exposed to the posited external wind. Near the core of an AGN host galaxy that retains a significant interstellar medium (ISM), the upwind jet may very well be isolated from the wind. Such details are beyond the scope of our current study.

The preceding simple analysis is illustrated in Figure 2. Curves plot the M_{hw} from Equation (11) (setting $\sqrt{A_j/A_h} = 0.7$). Values empirically determined from the 3D MHD parameter-matching simulations detailed in Section 3 have been added for comparison. The dotted horizontal line at $M_{hw} = 0$ corresponds to the condition for M_{wc} in Equation (12). The comparison simulated jets were initially in pressure balance with the pre-shock ICM ($P_j = P_i$) and had pre-shock Mach numbers, $M_{ji} = 3.5$, 5.0, and 7.5, matching the curves. They had a range of magnetizations and density contrasts with the ICM, as explained in Section 3.2. With the exception of two $M_{ji} = 3.5$ comparison simulations with $M_{si} = 3.5$ and 4, the simulations confirm the predictions of Equation (11). In both of the exceptional cases, the high post-shock pressure made the jet subsonic ($M_j < 1$), so that Equation (11) provides a poor approximation to M_{hw}. A better estimate would be $M_{hw} \sim -M_w + \sqrt{A_j/(\gamma A_h)}$, which is less than found from Equation (11) provided the trivial constraint on the pre-shock conditions, $\gamma M_{ji}^2 > 1$, is satisfied.

It is straightforward to estimate the shock strengths that lead the jets to become subsonic in the post-shock flow. In particular, using Equation (2) and assuming the post-shock jet pressure satisfies $P_j \sim P_w$, we conclude for $\gamma = 5/3$ that the jets in the post-shock flow become subsonic if

$$\frac{M_{si}}{M_{ji}} > \sqrt{\frac{4}{5} + \frac{1}{5M_{ji}^2}}. \quad (13)$$

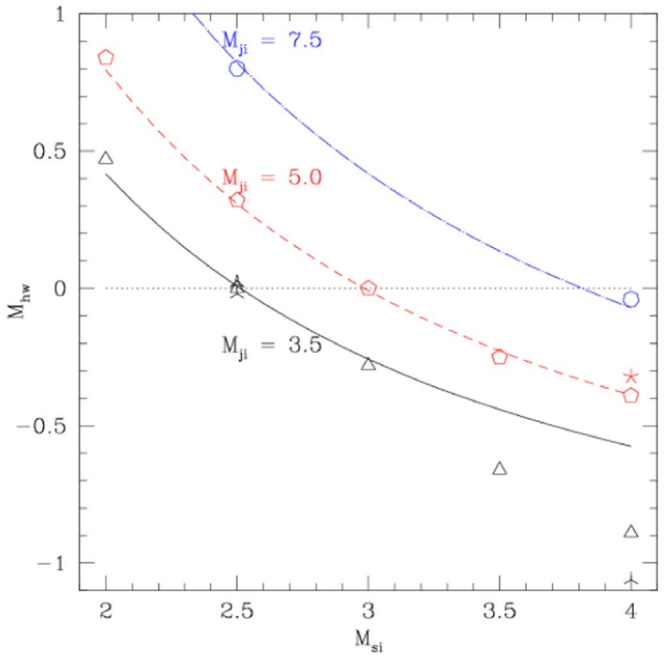

Figure 2. Upwind jet head advance Mach number, $M_{hw} = v_h/a_w$, in an aligned post-shock wind vs. incident shock Mach number, M_{si}. Curves represent Equation (11) with $\sqrt{A_j/A_h} = 0.7$ and post-shock conditions from Equations (2) and (5) for pre-shock jet Mach numbers $M_{ji} = 3.5$ (solid black), 5.0 (dashed red), and 7.5 (dashed blue). Points with colors matching the curves are empirically measured results from simulations with matching parameters (see Section 3). Point symmetries approximately reflect M_{ji} for the associated simulation. Values below the dotted horizontal line at $M_{hw} = 0$ indicate that the upwind jet head advance is reversed by the wind ($v_{hw} < 0$).

Although our focus in this paper is on winds that are aligned with the AGN jets, in Section 4.3 we briefly examine the situation in which a headwind effectively stops a jet that is moderately misaligned with the wind. In that case, it is more appropriate to describe the dynamical influence of the wind on the upwind AGN jet as a deflection or bending of the jet downwind rather than stopping the jet. In B. J. O'Neill et al. 2019a, in preparation, we explore generally how winds bend jets, but it is a convenient test of our analysis later in this paper to evaluate the condition identified in Equation (12) in terms of the deflection such a wind would produce if it were misaligned. In particular, we note that Equation (12) can be rewritten as $v_w^2 \rho_w = v_j^2 \rho_j (A_j/A_h)$. Then, if we recall the "classic" relation for the ratio of a jet radius to the bending radius of curvature, ℓ_b, in a transverse wind (Begelman et al. 1979; Jones & Owen 1979), $r_j/\ell_b \sim v_w^2 \rho_w/(v_j^2 \rho_j)$, we see immediately that Equation (12) corresponds roughly to the condition that a transverse wind would bend a propagating jet on a scale comparable to the jet radius. Thus, we would expect a wind satisfying Equation (12) impacting an oblique jet to very sharply deflect that jet. We confirm that behavior in a simulation outlined in Section 4.3 and in our analysis in B. J. O'Neill et al. 2019a, in preparation.

3. Simulation Specifics

3.1. Numerical Methods

The simulations reported here were carried out by employing the Eulerian WOMBAT ideal 3D nonrelativistic MHD code described in Mendygral (2011) on a uniform Cartesian grid using an adiabatic equation of state with $\gamma = 5/3$. The simulations utilized the second-order TVD algorithm with constrained magnetic field transport as in Ryu et al. (1998). The simulation setup specifics follow in Section 3.2.

The simulations also incorporated a conservative Eulerian Fokker–Planck solver for transport of the CRe distribution, $f(p)$, employing the "coarse-grained momentum volume transport" (CGMV) algorithm introduced by Jones & Kang (2005). The CGMV method provides an economical way to track CRe populations over a wide range of particle momenta (energies), including relevant physical processes. We outline here only a few essentials of the method, referring readers to Jones & Kang (2005) and references therein for further details. In the current simulations, the isotropic CRe momentum distribution, ($n_{\rm CRe} \propto \int p^2 f(p) dp = \int p^3 f(p) d\ln p$), was continuous in the range $10 \lesssim p/(m_e c) \lesssim 1.7 \times 10^5$ (so, energies $5\,{\rm MeV} \lesssim E_{\rm CRe} \lesssim 90$ GeV) with uniform logarithmic momentum bins, $1 \leqslant k \leqslant 8$. Within a given bin, k, the momentum distribution was assumed to be a power law, $f(p) \propto p^{-q_k}$, although q_k varied between bins. This distribution was evolved according to the history of a given CRe population. We included adiabatic, as well as radiative (synchrotron and inverse Compton), energy changes outside of shocks, along with test-particle diffusive shock (re)acceleration (DSA) at any shocks encountered. We did not include CRe energy losses from Coulomb collisions. For the thermal plasma densities relevant to these simulations, collisional losses are subdominant to inverse Compton/synchrotron losses unless $E_{\rm CRe} \lesssim 200\,{\rm MeV}$ (e.g., Sarazin 1999), whereas synchrotron emissions examined in this study generally involve $E_{\rm CRe} \gtrsim 1\,{\rm GeV}$. For $E_{\rm CRe} \lesssim 200\,{\rm MeV}$, the energy-loss timescales generally exceed the simulation times in any case.

We implemented DSA at shock passage by setting $q_{k,\rm out} = \min(q_{k,\rm in}, 3\sigma/(\sigma - 1))$ immediately post-shock, where σ is the code-evaluated compression ratio of the shock. This simple treatment is appropriate in the CRe energy range covered, since typical DSA acceleration times to those energies are much less than a typical time step in the simulations ($\Delta t \gtrsim 10^4$ yr). Our simulations primarily target lower-luminosity, Fanaroff & Riley class I (FRI) RGs (Fanaroff & Riley 1974) in which the relativistic plasma on multikiloparsec scales is energetically subdominant (e.g., Croston & Hardcastle 2014). Accordingly, our CRe populations were passive. The total CRe number density, $n_{\rm CRe}$, was arbitrary, since it had no impact on dynamical evolution. Consequently, we can compute meaningful synchrotron brightness, polarization, and spectral distributions from our simulations, but the synchrotron intensity normalizations that we present are arbitrary. Here we did not include spatial or momentum diffusion in our CRe and so neglected second-order turbulent particle reacceleration.

Except for a negligible background CRe population included in the ICM to avoid numerical singularity problems in the CGMV algorithm, all of the CRe in our simulations were injected onto the computational domain as part of the AGN jet generation process (outlined in the following subsection). At injection from the AGN source, the CRe momentum distribution was a power law with $q = q_0 = 4.2$ over the full momentum range. This translates into a synchrotron spectral index $\alpha = 0.6$ ($F_\nu \propto \nu^{-\alpha}$) using the conventional relation for power laws. Our synchrotron emissions reported here are computed using the actual $f(p)$ over the momentum range specified above, along with the full synchrotron emissivity

Table 1
Simulation Jet Parameters

Run	M_{ji} (v_{ji}/a_{ji})	ρ_i/ρ_j	v_{ji} (10^4 km s^{-1})	β_{pj} (P_i/P_{B0})	B_0 (μG)	θ_j^* (deg)	x_{jc} (kpc)	r_j (kpc)
J3S2	3.5	10^2	2.3	75	2.1	0	−80	3.0
J3S22	3.5	10^2	2.3	75	2.1	15	−288	3.0
J3S25a	3.5	10^2	2.3	10^3	0.6	0	−146	4.0
J3S25b	3.5	10^3	7.3	10^3	0.6	0	−146	4.0
J3S25c	3.5	10^2	2.3	10	5.8	0	−146	4.0
J3S3	3.5	10^2	2.3	10^3	0.6	0	−146	4.0
J3S35	3.5	10^2	2.3	10^3	0.6	0	−123	4.0
J3S4a	3.5	10^2	2.3	75	2.1	0	−208	3.0
J3S4b	3.5	10^3	7.3	10^3	0.6	0	−78	4.0
J5S2	5.0	10^2	3.3	10^3	0.6	0	−123	4.0
J5S25	5.0	10^2	3.3	10^3	0.6	0	−146	4.0
J5S3	5.0	10^2	3.3	10^3	0.6	0	−123	4.0
J5S35	5.0	10^2	3.3	10^3	0.6	0	−123	4.0
J5S4a	5.0	10^2	3.3	10^3	0.6	0	−78	4.0
J5S4b	5.0	10^3	3.3	10^3	0.6	0	−78	4.0
J7S25	7.5	10^2	5.0	10^3	0.6	0	−123	4.0
J7S4	7.5	10^2	5.0	10^3	0.6	0	−45	4.0

Note. All simulations had steady, bipolar jets launched from coordinate x_{jc} (with $y_{jc} = z_{jc} = 0$) in the x–y plane at $t = 0$ into a static, uniform, and unmagnetized ICM that had density $\rho_i = 5 \times 10^{-27}$ g cm^{-3} and pressure $P_i = 1.33 \times 10^{-11}$ dyne cm^{-2}, so sound speed $a_i = 667$ km s^{-1}. Here θ_j measures the angle between the jet axis and shock normal. At launch, the jets had (gas) pressure $P_j = P_i$, so internal sound speed $a_{ji} = a_i\sqrt{\rho_i/\rho_j}$. In all reported simulations, $\Delta x = \Delta y = \Delta z = 0.5$ kpc.

kernel for isotropic electrons, given a local magnetic field $\boldsymbol{B}$ (e.g., Blumenthal & Gould 1970).

3.2. Simulation Setup

For this study, we carried out 16 3D MHD simulations involving bipolar AGN jets. With one exception, the jet axis aligned with the normal of an incident plane ICM shock. In one simulation, the jet axis was offset by 15° from the shock normal. The simulation parameters are outlined in Tables 1 (jet properties) and 2 (shock and ICM properties). These simulations cover a range of internal jet Mach numbers of $3.5 < M_{ji} < 7.5$ and external ICM shock Mach numbers of $2 < M_{si} < 4$. The jet and shock Mach numbers provide the basis for labeling the various simulations. For example, the simulation J3S2 involved jet Mach number $M_{ji} = 3.5$ and shock Mach number $M_{si} = 2$ (keeping only one digit of the Mach number in the label). In several cases where we considered multiple shock Mach numbers between integer values, we added a second digit to the shock Mach number in the label. For instance, simulation J3S2 involved $M_{si} = 2.0$, while simulation J3S22 involved $M_{si} = 2.25$. In three situations where we varied either the jet density or magnetic field strength (always maintaining the jet gas pressure, $P_j = P_i$, and jet Mach number, M_{ji}, at launch), we added the letter "a," "b," or "c" at the end of the label. For example, simulations J3S4a and J3S4b both involved $M_{ji} = 3.5$ and $M_{si} = 4$ but had β_{pj} values of 75 and 10^3, respectively. Our detailed analysis in Section 4 focuses primarily on two aligned shock–jet simulations, J3S2 and J3S4a, that roughly span the range of dynamical behaviors we obtained. The specifics of those simulation properties are emphasized in Tables 1 and 2. Section 4 also includes a brief comparison of J3S22, which breaks the alignment symmetry of the other simulations. The simulation domains, while varying in size according to the needs of a given dynamical situation, were all rectangular prisms with the origin at the domain center ($x = y = z = 0$). All grid boundaries in the simulations were open, except for inflow conditions fixed at the left x boundary to drive the planar ICM shock in the $+x$ direction.

Table 2
Simulation Shock and Domain Parameters

Run	M_{si}	P_w/P_i	v_w (10^3 km s^{-1})	$x_{\rm domain}$ (kpc)	$y_{\rm domain}$ (kpc)	$z_{\rm domain}$ (kpc)
J3S2	2.0	4.75	0.75	±320	±149	±149
J3S22	2.25	6.08	0.90	±464	±240	±144
J3S25	2.5	7.56	1.05	±224	±50	±50
J3S25b	2.5	7.56	1.05	±224	±50	±50
J3S25c	2.5	7.56	1.05	±224	±50	±50
J3S3	3.0	11.0	1.33	±224	±50	±50
J3S35	3.5	15.1	1.61	±224	±50	±50
J3S4a	4.0	19.8	1.88	±448	±149	±149
J3S4b	4.0	19.8	1.88	±224	±50	±50
J5S2	2.0	4.75	0.75	±224	±50	±50
J5S25	2.5	6.08	1.05	±224	±50	±50
J5S3	3.0	11.0	1.33	±224	±50	±50
J5S35	3.5	15.1	1.61	±224	±50	±50
J5S4a	4.0	19.8	1.81	±224	±50	±50
J5S4b	4.0	19.8	1.81	±224	±50	±50
J7S25	2.5	7.56	1.05	±224	±50	±50
J7S4	2.0	19.8	1.88	±224	±50	±50

Note. In all simulations, shocks entered the domain from the $-x$ boundary propagating in the $+\hat{x}$ direction. The post-shock "wind" velocity, v_w, is computed from Equation (3), while P_w is from Equation (2). In all reported simulations, $\Delta x = \Delta y = \Delta z = 0.5$ kpc.

All of the simulated AGN jets reported here were steady, as well as collimated and bidirectional at launch, beginning by definition at $t = 0$. They were launched out of a cylinder whose

axis was in the x–y plane and at rest on the grid, centered at the middle of the y–z plane ($y = z = 0$). In all but one of the simulations, the jet axis was along the grid x-axis to align with the external shock propagation. The central x-coordinate for the jet launch cylinder, x_{jc}, was adjusted for each simulation according to dynamical parameters to delay boundary interactions associated with the jets as long as practical (specifics are given for each simulation in Table 2).

Jet launch cylinders were 24 grid cells long, with similar jets emerging from each end. They had radii of either six or eight cells, as indicated in Table 1. The launch cylinders were surrounded by a coaxial cylindrical collar two grid cells thick providing a transition from the conditions maintained inside the launch cylinder to the ambient conditions outside. Our launched jets were dynamically composed of nonrelativistic (thermal), weakly magnetized ($\beta_{pj} \gg 1$, as defined below) plasma, since we have in mind FRI jets that, on these scales, have entrained substantial ISM plasma from their galaxies of origin (e.g., Croston et al. 2018). As noted above, we included a passive, relativistic CRe population in order to model nonthermal emissions. To directly trace the distribution of plasma injected onto the grid through the jet launch cylinder, we advected a passive "jet mass fraction" scalar that was set to unity for material entering the grid via the jet launch cylinder but initialized at zero elsewhere.

The simulated jets were magnetized inside the launch cylinder by a uniform, poloidal electric current whose sign matched the jet velocity at a given location. The result was a toroidal magnetic field inside the launch cylinder, $\boldsymbol{B} = \pm B_0(r/r_j)\hat{\phi}$, where r_j is the outer jet radius, and $\hat{\phi}$ is the azimuthal unit vector relative to the launch cylinder axis. The nominal jet magnetic field strength, $B_0 = B(r_j)$, was set by fixing the plasma $\beta_{pj} = P_i/P_B(r_j)$ at the launch cylinder perimeter, r_j, where $P_B(r_j) = B_0^2/(8\pi)$ is the magnetic pressure at r_j. For the simulations reported here, β_{pj} ranged between 10 and 10^3, as listed in Table 1. There was a poloidal return current in the launch cylinder transition collar, so the net electric current along the jet launch cylinder vanished everywhere. The ambient ICMs, both undisturbed and post-shock, were initially unmagnetized in all of the simulations reported here. Of course, any ambient ICM that mixed with jet plasma became magnetized and carried CRe originating in the jets. We acknowledge that real ICM plasmas are magnetized, but our approach maximizes our ability to understand how AGN magnetic fields evolve in response to the dynamical scenarios under study.

The emergent jet density ρ_j, gas pressure $P_j = P_i$, and velocity $v_j = M_{ji}a_{ji}$ were uniform across the ends of the launch cylinder, where $a_{ji}^2 = \gamma P_i/\rho_j = \rho_i/\rho_j\, a_i^2$. The simulations reported here mostly set $\rho_i/\rho_j = 10^2$, but we also included two cases with $\rho_i/\rho_j = 10^3$. The $\rho_i/\rho_j = 10^2$ contrast is a compromise that allows for a light jet while keeping the simulation cost reasonable. Although detailed lobe morphology varies with ρ_i/ρ_j, the dynamical behaviors at the center of this study—namely, the propagation of the RG head and the interaction of the jets with the post-shock wind—were insensitive to this ratio (see, e.g., Figure 2). Due to these density ratios, either $a_{ji} = 10a_i$ or $a_{ji} \approx 31.6a_i$. The launched jet Mach number $M_{ji} = 3.5$ in our detailed analysis simulations J3S2 and J3S4a, but in other simulations, it ranged between 3.5 and 7.5, as indicated in Table 1. All of the simulations reported here included plane shocks propagating through the stationary, homogeneous ICM along the x-axis, entering from the left boundary. The ICM shock Mach numbers, M_{si}, ranged between 2 and 4, as indicated in Table 2.

Up to this point in our presentation, we have provided no explicit physical length, time, density, or pressure scales for the simulations. That is because, except for radiative energy losses by the passive CRe, the simulations are scale-free, meaning none of the dynamical outcomes in our simulations depend on those choices. In particular, since the fluids are ideal, adiabatic, and nonrelativistic, all of the dynamical behaviors can be fully referenced to dimensionless parameters, such as Mach number β_{pj} and ambient-to-jet density ratio, and normalized by a characteristic length, such as r_j; a characteristic pressure, such as P_i; and a characteristic velocity, such as a_i. We do this purposefully, so that readers can choose the scales that best suit their specific purpose. However, since we do include radiative behaviors of the CRe at specified frequencies in order to identify observable behaviors, representation of the CRe populations and their associated emissions requires us to explicitly identify length, velocity, and magnetic field scales. On the latter point, we emphasize that the magnetic field and pressure scales are uniquely linked by β_{pj}. In addition, since CRe radiative losses include inverse Compton scattering of cosmic microwave background photons, and that is a function of redshift, emissions analysis requires us to also specify redshift. For the simulations reported here, we set the redshift to be $z = 0.2$, for which the inverse Compton radiative cooling time $\tau_{\rm rad} \sim 60\,(10\,{\rm GeV}/E_{\rm CRe})\,{\rm Myr}$, where $E_{\rm CRe} = pm_e c$ is the CRe energy. For $z \to 0$, the inverse Compton cooling time at a given CRe energy is approximately doubled. The angle-averaged synchrotron energy-loss rate matches the inverse Compton rate for $B \approx 3.25\ \ (1+z)^2\ \mu{\rm G}$, approximately corresponding to $4.7\ \mu$G at $z = 0.2$. In the source frame, the synchrotron critical frequency can be expressed as $\nu_c \approx 1.7\,{\rm GHz}\,(E_{\rm CRe}/10\,{\rm GeV})^2 B_{\ \mu{\rm G}}$. We found that our dynamical results were relatively insensitive to β_{pj} within the range we explored, so with appropriate rescalings of emission frequency and/or radiative lifetimes (while properly accounting for inverse Compton cooling), our synchrotron emission images could be adjusted relatively simply for different β_{pj} choices.

In practice, we set our simulation length scale so that a grid cell spanned $\Delta x = \Delta y = \Delta z = 0.5\,{\rm kpc}$. Our jet launch cylinder length was then 6 kpc from the center to each end. At launch, the jets had $r_j = 3$ or 4 kpc, depending on the number of cells radially spanning the launch cylinder. The characteristic ICM pressure and sound speed were $P_i = (4/3) \times 10^{-11}\,{\rm dyne\,cm^{-2}}$ and $a_i = (2/3) \times 10^3\,{\rm km\,s^{-1}} \approx (2/3)\,{\rm kpc\ Myr^{-1}}$, respectively, so that $\rho_i = 5 \times 10^{-27}\,{\rm g\,cm^{-3}}$. All of our simulations included uniform pre-shock ICMs with these properties. While this is, of course, a dramatic simplification from real cluster environments, this choice helps us to identify the physical behaviors resulting from the dynamical scenario under study and not due to complications from additional structure in the medium. With these characteristic scalings, the jet magnetic field strength parameter $B_0 = \sqrt{8\pi P_i/\beta_{pj}} \approx 18\ \mu{\rm G}/\sqrt{\beta_{pj}}$, so B_0 ranged from about 0.6 μG ($\beta_{pj} = 10^3$) to about 6 μG ($\beta_{pj} = 10$). Consistent with our scalings in the previous paragraph, CRe synchrotron energy losses are subdominant to inverse Compton energy losses at $z = 0.2$, unless $B \gtrsim 4.7\ \mu$G. Thus, except in flow regions where the magnetic field became significantly

amplified by stretching, nonadiabatic CRe energy losses were dominated by inverse Compton cooling, which is uniform in time on the scales relevant to these simulations. If our simulated objects were moved to redshift $z = 0$, the minimum magnetic field required for synchrotron losses to dominate inverse Compton losses would drop to 3.3 μG. The CRe reacceleration at shocks via DSA, as well as adiabatic energy changes, were included, although only a few of the strongest shocks that developed in these simulations were strong enough to significantly influence the "observed" synchrotron emissions.

4. Discussion

We now examine and compare three of the simulations from Tables 1 and 2. Our primary focus is on two of these, namely, J3S4a and J3S2, which span the behaviors of our aligned jet ($\theta_j = 0$) simulations. In order to illustrate the consequences of moderate misalignment between the AGN jets and the ICM shock normal, we also briefly discuss the "misaligned" simulation J3S22 with $\theta_j = 15°$. All three simulations involved AGN jets with Mach number $M_{ji} = 3.5$, jet mass density $\rho_j = 10^{-2}\rho_i$, and characteristic magnetic field strength $B_0 = 2.1$ μG. The only significant difference between the two aligned simulations, J3S4a and J3S2, was the ICM shock Mach number. In J3S4a, $M_{si} = 4.0$, while in J3S2, the shock had $M_{si} = 2.0$. The shock in J3S22 had $M_{si} = 2.25$, which we had estimated in advance as capable of just stopping the advance of the upwind AGN jet, taking into account that some of the jet momentum was in the $\hat{y}$ direction, as an $M_{si} = 2.5$ shock would be required for an aligned jet with the same properties (see Equation (12); Figure 2).

In all three simulations, slightly more than 50 Myr of steady, undisturbed AGN evolution passed before shock first contact. The properties of the RGs at initial shock contact were, accordingly, quite similar. In particular, during this pre-shock evolution, each jet head advanced into the ICM with Mach number $M_{ho} = v_{ho}/a_i \approx 2.5$, consistent with Equation (10) using $M_w = 0$ and $\sqrt{A_j/A_h} \approx 0.7$ ($A_h/A_j \approx 2$). At first shock contact, each of the RG lobes had a length of ~90 kpc. We note that although the detailed shapes of the RG lobes in our simulations depended on the density ratio,[5] ρ_j/ρ_i, the velocity of the jet heads, and thus the lengths of the RG lobes, did not depend on ρ_j/ρ_i.

Because of their near-axial symmetry, the post-shock evolution of both J3S4a and J3S2 was simpler than that of J3S22, though all three were qualitatively consistent with the dynamical scenario outlined in Section 2. In particular, the incident shocks propagated rather quickly through the low-density RG lobes and generated recognizable vortex ring structures. The upwind jet in J3S4a was strongly reversed in the post-shock wind, and, as predicted for these parameters in Section 2.2, the AGN jets in J3S4a actually became subsonic in this flow.[6] The upwind jet in the misaligned case, J3S22, was sharply bent in the downwind direction, although it remained supersonic. The upwind jet in J3S2 continued to advance into the post-shock wind at a speed, v_{hw}, consistent with Equation (11).

4.1. Simulation J3S4a: $\theta_j = 0$, $M_{ji} = 3.5$, $M_{si} = 4.0$

The dynamical RG evolution of the J3S4a RG–shock encounter is outlined in Figure 3. The figure presents four snapshots of the volume-rendered[7] jet mass fraction tracer (left panels) and mass density (right panels) at (1) $t = 46$ Myr, just prior to RG–shock first contact (refer to Figure 1 for the geometry); (2) $t = 92$ Myr, after the post-shock flow reversed the upwind AGN jet; (3) $t = 230$ Myr, after the shock-generated vortex ring became fully developed and, as discussed in Section 2.1, had just pinched off, and thus truncated, the downwind jet; and (4) $t = 492$ Myr, after the ICM shock and the vortex ring (advected in the post-shock wind) left the simulation box to the right. The structures remaining in the computation domain at the latest time were very close to what would result from a pure head-on wind with the same properties but absent any shock impact. We note that for $t \gtrsim 92$ Myr, the RG itself became essentially a one-sided jet outside the jet launch cylinder. This outcome should follow as long as the jet and wind combine to satisfy the dynamics reflected in Equation (12).

At $t = 92$ Myr, the accelerated internal shock had propagated fully through both lobes, while the much slower external shock (outlined in dashed gray in the left panels of Figure 3 and emphasized in the density images on the right by enhancing the emissivity of the shock in the external medium) had just passed the position of the AGN (marked with a red cross). The external ICM shock in this simulation propagated substantially faster than the pre-shock downwind RG head ($M_{si} = 4$ versus $M_{ho} \approx 2.5$). Consequently, by $t = 230$ Myr, the external ICM shock had reached almost as far as the shock-modified RG, then extended downstream. It was located just to the right (downstream) of the vortex ring visible in the mass fraction rendering. The convex shock structure visible to the right of the external ICM shock in the density rendering highlights the location of the accelerated internal shock after it exited the RG downwind lobe ahead of the external shock. The vortex ring–induced high mass density region mentioned in Section 2.1 and surrounding the jet just to the left (upstream) of the vortex ring is also obvious at $t = 230$ Myr. Thermal bremsstrahlung images we constructed (not shown) indicated an enhanced X-ray flux of ~22% from this region. This suggests such high-density features developed from shock-induced vortex structures could be detectable during this stage in deep X-ray ICM images. We leave exploration of this effect and its observational signatures to future work.

The jet mass fraction rendering at $t = 230$ Myr clearly reveals the vortex ring. It is also obvious from the mass fraction view at this time that the right-facing downwind jet, having recently been pinched off by circulation of the vortex ring, no longer continued to the extreme downwind RG extension. However, since the AGN was still active, the truncated downwind jet terminus visible just to the left of the vortex ring continued to drive downwind (to the right). But the now-subsonic jet, rather than forming a new RG lobe extending well back toward the AGN, was surrounded at its terminus by a more limited "proto-lobe" of AGN plasma. The strong post-shock wind prevented that plasma from extending a substantial

[5] The pre-shock lobes in simulations J3S25b and J3S4b with $\rho_j/\rho_i = 10^{-3}$ were fatter than the lobes in simulations with $\rho_j/\rho_i = 10^{-2}$, such as J3S4a and J3S2.

[6] We verified in other simulations that an equivalent wind without shock impact led to essentially the same jet propagation properties, including its subsonic character.

[7] As viewed along the $\hat{z}$-axis at a distance roughly 1.5 Mpc from the AGN.

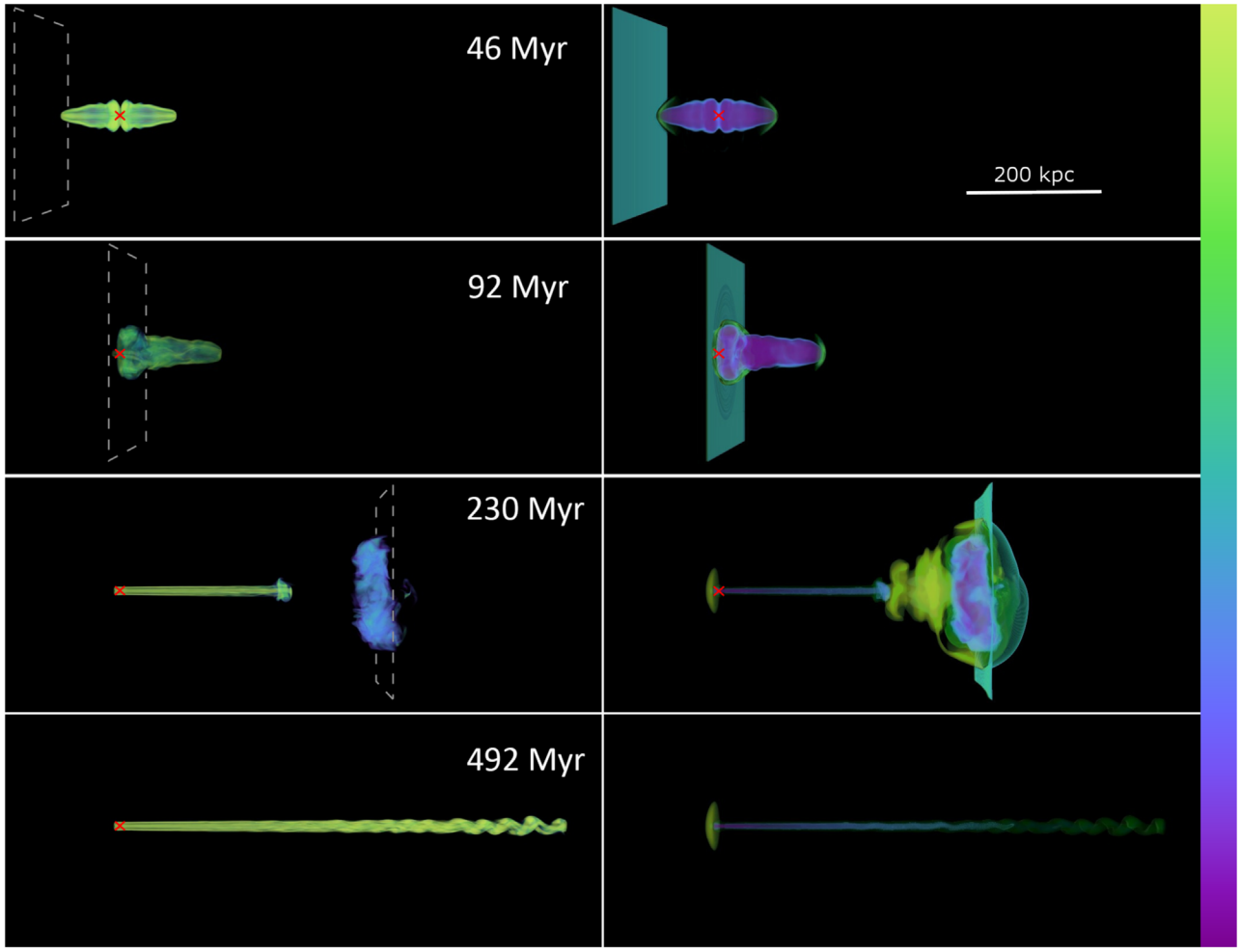

Figure 3. Volume renderings of the J3S4a simulation at four times, increasing from top to bottom. The shock normal and jet axis are in the viewing plane. Shock impact on the RG began soon after the top snapshot. Left: jet mass fraction (>30% visible). Right: log mass density spanning 3 decades in ρ, with key dynamical structures highlighted. The external ICM shock is outlined in dashed gray in the left images, while it can be directly observed in the right images. Colors in all images follow the "CubeYF" color map, with "yellow" high and "purple" low. The AGN location is marked in each image by a red cross.

distance back toward the AGN. That is, it never formed a classic RG lobe. It is, nonetheless, a distinct backflow feature from the AGN jet. We point out below that the magnetic field in this proto-lobe was relatively strong, and, consequently, it was remarkably radio-bright (see Figures 4–6).

Since pinching or otherwise disrupting the downwind AGN jet by the vortex circulation produced distinctive features, it is appropriate to outline the essential conditions required for this development. As mentioned in Section 2.1, the excess "on-axis" pressure toward the perimeter of the ring vortex is $P_{ex} \sim \rho_i v_{\rm CD}^2 \gtrsim M_{si}^2 \rho_i a_i^2$, where $v_{\rm CD} > v_{si}$ is the speed at which the CD between RG lobe plasma and post-shock ICM plasma propagated through a lobe. Disruption of the propagating jet by such a pressure imbalance across it would require roughly that $P_{ex} \gtrsim \rho_j v_j^2$. This leads to a very rough condition estimate for disruption of the jet by the vortex flow, $M_{si} \gtrsim M_{ji}$. That is, when the ICM shock Mach number is comparable to or exceeds the Mach number of the AGN jet in the pre-shock flow, the chances are high that the downwind jet may be disrupted by the flow of the vortex ring. In J3S4a, that condition is easily satisfied.

Additional insights into the dynamical evolution of J3S4a are evident in Figure 4, which presents volume renderings of the magnetic field strength at the middle two times in Figure 3.

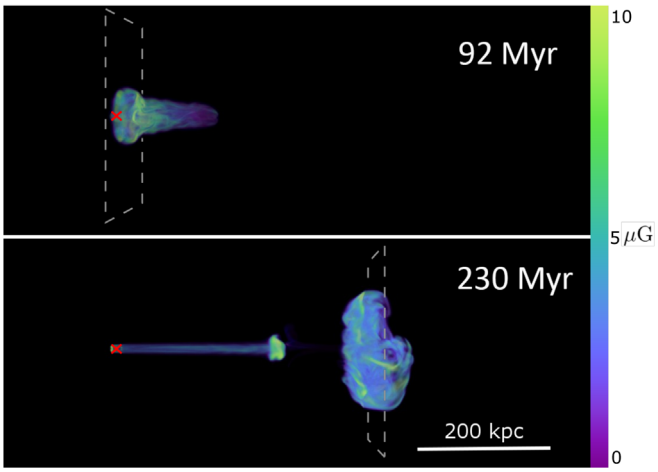

Figure 4. Volume rendering of magnetic field intensity in the J3S4a simulation at the two intermediate times and the same perspective as in Figure 3. The emergent AGN jet carries a peak 2 μG field into an unmagnetized ICM. The fields visible in the image span roughly 1 to 10 μG. As in Figure 3, the location of the external ICM shock is outlined in gray.

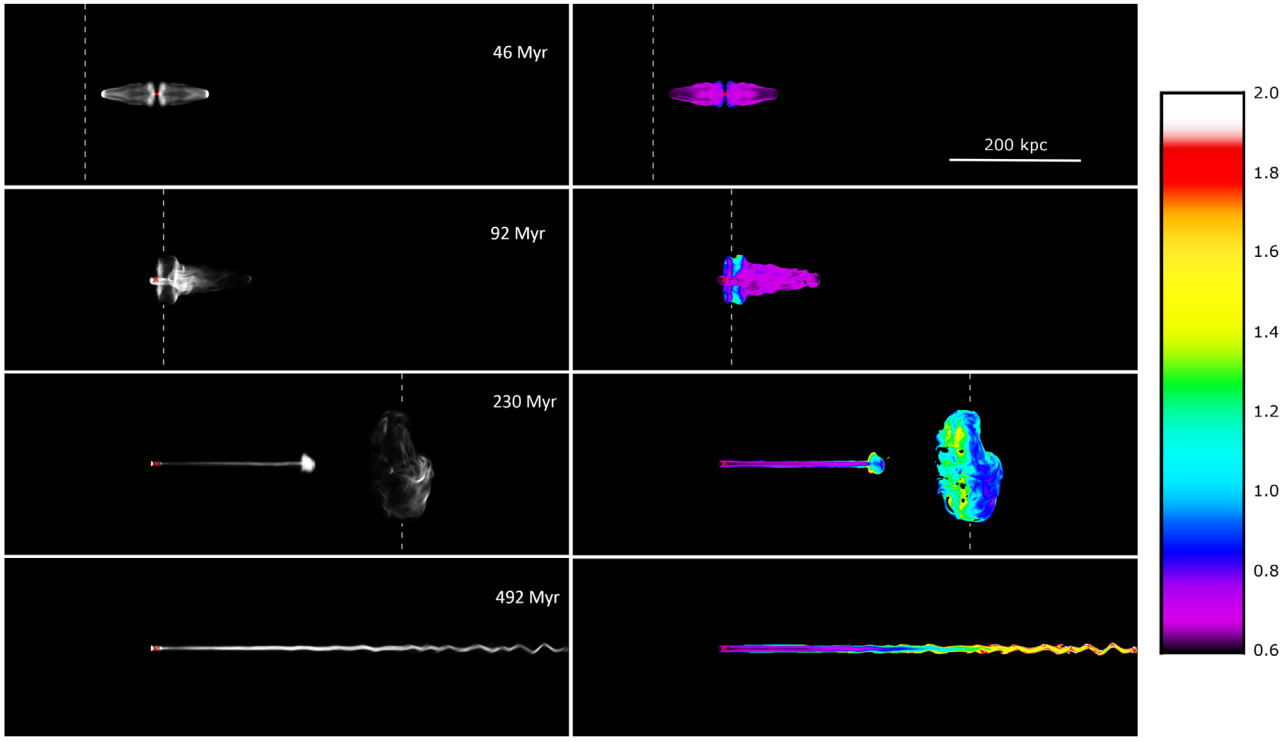

Figure 5. Synchrotron images from J3S4a at the times in Figure 3. Resolution is 0.5 kpc. The AGN jet axis and shock normal are in the plane of the sky. Left: 150 MHz intensity with the brightest pixel in each image approximately the highest intensity excluding the jet launch cylinder at that time. Right: 150/600 MHz spectral index, $\alpha_{150/600}$, for regions above 0.5% of the peak intensity at 150 MHz. The spectral index scale is on the far right. At launch, the jet spectral index was $\alpha = 0.6$. The location of the external ICM shock is denoted by a dashed gray line.

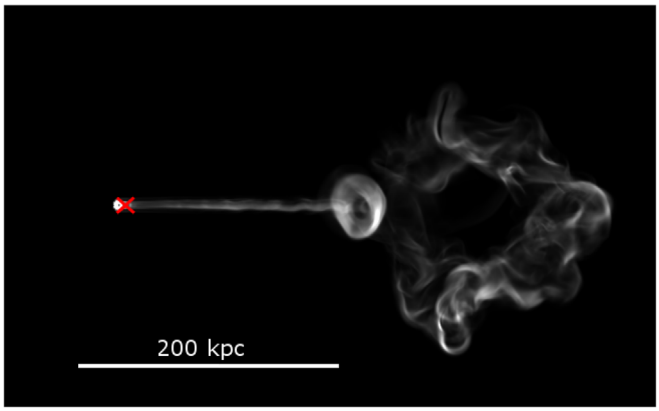

Figure 6. The 150 MHz synchrotron image from J3S4a at $t = 302$ Myr with the downwind jet axis projected away from the observer and 30° from the line of sight in order to reveal the ring nature of the vortex ring produced by the shock impact and the "proto-lobe" at the terminus of the truncated downwind jet.

Recall that the ambient ICM was unmagnetized in this simulation, while the peak magnetic field in the emergent jets was $B_0 \approx 2\,\mu$G. The "naked" jet visible in the lower, later image in the figure exhibited fields close to those emergent strengths. In fact, to a large degree, the magnetic field in the jet retained its original toroidal form to very large distances. However, there were substantial regions in the vortex ring, both as it was first forming (see $t = 92$ Myr in the figure) and after it had separated from the AGN (see $t = 230$ Myr in the figure), where the field strengths reached and even exceeded 10 μG in filaments evidently spanning the torus. The same is true in the proto-lobe at the end of the truncated downwind jet visible at $t = 230$ Myr.

The dynamical link to the development of these strong fields is that those structures contain strong vortical motions that have stretched and amplified the magnetic field originally coming from the jets. In fact, the rms magnetic field strength in the vortex ring continued to increase until the structure exited the computational domain just after $t \sim 302$ Myr. The peak magnetic field in the proto-lobe also increased with time, although the rms field did not change significantly. There were, additionally, magnetic field regions in the RG lobes amplified by shear prior to the shock encounter, although the strong shock-induced shear was much more effective in this regard. Since significant ICM plasma was entrained into the lobes as well as the vortex ring, had our ICM been magnetized, the fields in all of these regions would likely have been stronger than we see here (see, e.g., Tregillis et al. 2001; O'Neill et al. 2005; Huarte-Espinosa et al. 2011).

Figure 5 presents 0.5 kpc resolution radio synchrotron images of the J3S4a structures at the same times as in Figure 3. The plane of the sky includes the AGN jets and ICM shock normal. Each image is integrated from the synchrotron emissivity along the line of sight. The left panels show the synchrotron brightness (arbitrary units) at 150 MHz, while the right panels show the associated 150/600 MHz spectral index maps for the emission down to 0.5% of the peak 150 MHz intensity in each image. As a reminder of the "doughnut" toroidal topology of the vortex ring structure, we also show in Figure 6 the 150 MHz image of J3S4a at $t = 302$ Myr with the downwind jet axis and the shock normal now projected 60° from the plane of the sky.

Two key things are immediately evident from the intensity images. First, the synchrotron surface brightness in this frequency band for this source traces very well the regions of

strong magnetic field amplification (see Figure 4). At the earliest time shown ($t = 46$ Myr), the field amplification in the unshocked lobes mentioned above is particularly visible in the central regions near the jet source. Second, at late times, when it was the only dynamical structure linked to the AGN, the downwind jet remained moderately bright at these frequencies over distances approaching Mpc scales. At the latest time shown ($t = 492$ Myr), when only the jet remained in the simulation domain, the jet surface brightness actually peaked more than 100 kpc from its source. We note that the synchrotron image at this time is at least qualitatively reminiscent of the one-sided tail, "source C," in A2256 in both scale and form (Owen et al. 2014). In considering this comparison, it is worth keeping in mind that many properties of the simulated AGN at this time, after the vortex ring has been advected away, are predominantly controlled by the jet interactions with the surrounding wind. The primary role of the incident shock at this stage is its generation of the strong, high-pressure wind. But any dynamics capable of setting up such a relative wind would lead to rather similar behaviors.

The spectral index images in Figure 5 add useful insights to the surface brightness behaviors for J3S4a. In particular, $\alpha_{150/600}$ remains close to the source value, $\alpha = 0.6$, in regions still "in direct communication with" the AGN until the last image at $t = 492$ Myr. At the three earlier times ($t = 46$, 92, and 230 Myr), only plasma that was or had been wrapped into the vortex ring (i.e., isolated from the jets) showed clear evidence of spectral steepening (aging) in this band. At $t = 492$ Myr, when only the downwind jet remained in the domain, the jet spectrum remained reasonably flat over much of its length, with $\alpha_{150/600} \lesssim 1$ over a distance out to roughly 1/2 Mpc from the source. Near where the jet exited the computational domain, however, $\alpha_{150/600} \gtrsim 1.5$. It should be noted that CRe aging in this tail was influenced at a given distance from the AGN by the fact that the relatively low Mach number of the launched jet in this simulation, $M_{ji} = 3.5$, combined with the high pressure in the strong post-shock wind, caused the jet to become subsonic relatively slower than at launch. A jet with an initially higher Mach number would have remained supersonic to the end (see Section 2.2).

In general, the modest aging behaviors just described are consistent with the fact that, in much of the visibly emitting volume in this source, $B < 5\ \mu$G. There, CRe aging was dominated by inverse Compton cooling (recall that $z = 0.2$). At the same time, in most of the synchrotron-visible regions, $B \geqslant 1\ \mu$G, so synchrotron emissions at frequencies $\lesssim$1 GHz came from CRe with $E_{\rm CRe} \lesssim$ few GeV. Under these circumstances, CRe radiative lifetimes, $\tau_{\rm rad} \gtrsim 100$ Myr. As emphasized above, the magnetic field strengths in the vortex ring and the proto-lobe feature sometimes reached or exceeded $B \sim 10\ \mu$G, which not only made those structures bright but also reduced $\tau_{\rm rad}$ to something closer to 30 Myr for CRe emitting near 1 GHz. That explains why, in Figure 5, the spectra in those features are relatively steeper than in some other bright regions.

The behaviors just outlined facilitate interpretation of the integrated synchrotron spectrum and its evolution as shown at multiple times in Figure 7 between $t = 46$ and 302 Myr. We see in particular that, prior to formation of the vortex ring between $t = 92$ and 131 Myr, the integrated luminosity grows at a faster-than-linear pace, due in combination to continued fresh CRe injection from the AGN and moderate magnetic field amplification. At the same time, the spectrum maintains close to the injected spectral index, $\alpha = 0.6$, at low frequencies and exhibits very modest shape evolution due to aging. Once the plasma in the vortex ring is disconnected from the AGN prior to $t = 131$ Myr, the integrated spectrum starts to age significantly.

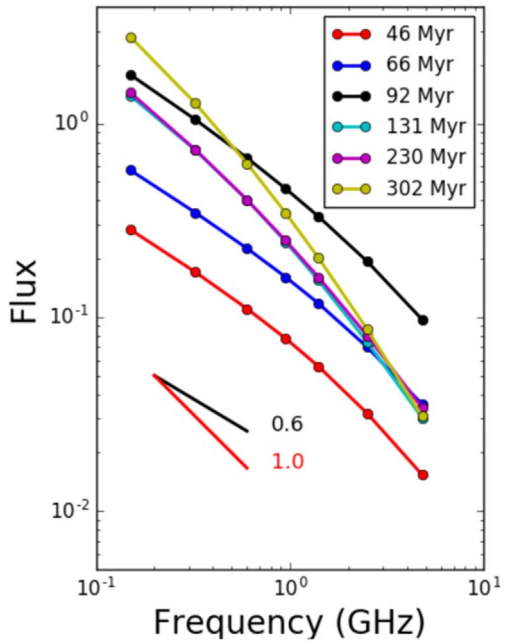

Figure 7. Evolution of the full, integrated J3S4a synchrotron spectrum before the vortex ring left the grid. Power-law spectra with $\alpha = 0.6$ and 1.0 are shown for comparison.

The importance of the vortex ring to the integrated properties is apparent in Figure 8, where the total flux at three times ($t = 164$, 230, and 302 Myr) has been separated into contributions from the vortex ring and everything else (the "jet" in the labels). It is clear that the spectrum of the vortex ring became significantly steeper and more convex over time compared to the emissions coming from regions still in communication with the AGN. It is also notable that, except at high frequencies, the total flux from the vortex ring is generally greater than the remainder of the source. That is a consequence of the continued magnetic field amplification in the vortex ring, which persisted in the simulation until the vortex ring left the computational domain. We did not include turbulent CRe reacceleration in this simulation, but that would likely have enhanced the radio luminosity of the vortex ring even further while reducing spectral aging. The details of those rather uncertain processes are beyond the scope of this study.

4.2. Simulation J3S2: $\theta_{\rm j} = 0$, $M_{\rm ji} = 3.5$, $M_{\rm si} = 2.0$

Figure 9 presents volume renderings of the jet mass fraction (left) and log mass density (right) from the J3S2 simulation at times $t = 119$ and 270 Myr. Recall that the only significant difference between the J3S2 and J3S4a simulations was the strength of the incident ICM shock along with its associated post-shock wind. Although both shock impacts have obvious consequences, the weaker shock in this case ($M_{si} = 2$) has less immediately obvious dynamical influence on the RG than the $M_{si} = 4$ shock in J3S4a. In both cases, shock interaction with the RG began just after $t = 50$ Myr. Qualitatively, the dynamical state at $t = 119$ Myr in Figure 9 is similar to the

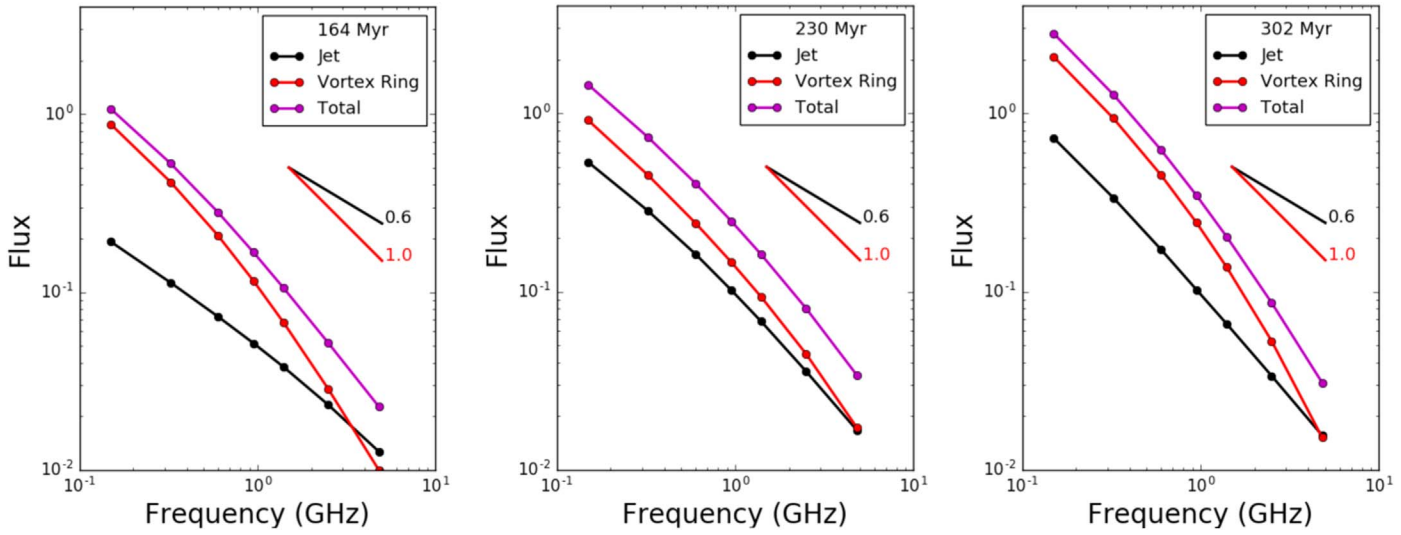

Figure 8. Late evolution of the J3S4a synchrotron spectra isolating contributions from the disconnected vortex ring.

$t = 92$ Myr state after the stronger shock impact shown in Figure 3. Noting that a cross marks the location of the AGN in each case, however, it is already evident that the weaker shock in J3S2 has not completely stopped the advance of the upwind AGN jet. This is in contrast to the situation in J3S4a, where the upwind jet was reversed. The rate of upwind head advance in J3S2 is, on the other hand, consistent with Equation (11), as shown in Figure 2. Indeed, it is obvious that the upwind jet at $t = 270$ Myr in the lower panel of Figure 9 has extended its length since the earlier time in the upper panel. A compact AGN plasma cocoon (RG lobe) also remains around the upwind jet.

The dynamical distinctions between J3S2 and J3S4a are even more obvious on the downwind side, especially at later times. For instance, in Figure 9, it is apparent that the $M_{si} = 2$ external (ICM) shock at $t = 270$ Myr in J3S2 was ~200 kpc behind the downwind jet head. In contrast, at the earlier $t = 230$ Myr, the $M_{si} = 4$ external shock in Figure 3 was overtaking the full downwind RG structure, and the vortex ring formation had disrupted the downwind jet propagation. In fact, the external ICM shock in J3S2 never did overtake the end of the downwind jet during the simulation. Figure 9 reveals that a vortex ring surrounded the downwind RG lobe, and a high-pressure, high-density region surrounded the downwind jet at $t = 270$ Myr. There was also substantial ICM plasma inside the downwind lobe, carried forward by the shock internal to the cavity. However, it remains clear that neither the jet nor the downwind lobe had been disrupted. As a consequence, and again in contrast to J3S4a, the vortex ring never developed into an isolated structure.

Additional similarities and differences between J3S2 and J3S4a can be seen by comparing the magnetic field volume renderings in Figures 10 and 4. In both cases, peak magnetic field strengths several times greater than those in the jets resulted from stretching by vortical motions. Allowing for differences in jet behaviors, the magnetic field distribution at $t = 119$ Myr in J3S2 was qualitatively similar to that at $t = 92$ Myr in J3S4a. In particular, both cases exhibit substantial magnetic field amplification in their nascent vortex ring structures, along with more modest field enhancements in the RG lobes. But, again at the later times ($t = 270$ Myr in Figure 10 and $t = 230$ Myr in Figure 4), the differences from the relative rate of shock propagation and the strength of the vortex ring in the two simulations are obvious. Both RG lobes in Figure 10 exhibited substantial magnetic field amplification by this time. In contrast, and as described above, the upwind side of J3S4a was completely absent, and the downwind jet in J3S4a had been disrupted well before this time by formation of the vortex ring. The J3S4a vortex ring was by then isolated from the AGN and being advected away by the post-shock wind. One of the most obvious regions of amplified magnetic field in the downwind region of J3S4a at late times was, in fact, the vortex ring.

Figure 11 illustrates the synchrotron surface brightness images of J3S2 at 150 MHz, along with the associated $\alpha_{150/600}$ spectral distributions at $t = 119$ and 270 Myr. It is remarkable, given the evidence in Figure 10 for substantial magnetic field amplification in the downwind (right side) RG lobe, that the 150 MHz surface brightness from that structure was mostly relatively low at both times shown. In fact, at $t = 270$ Myr, the downwind jet exhibited significantly higher surface brightness than the lobe on that side, despite the relatively weaker magnetic field in the jet. Indeed, although some volumes in J3S2 with strongly amplified magnetic fields were radio-bright, such as the nascent vortex ring at $t = 119$ Myr and the upwind lobe at $t = 270$ Myr, the 150 MHz surface brightness was not a consistent indicator of magnetic field strength patterns. This is in contrast to what we found for J3S4a.

Several features revealed in Figure 9 and the right side of Figure 11 combine to explain this different result. Looking first at Figure 9, we see that at both times, but especially at the later time, the jet mass fraction distribution in the downwind lobe of J3S2 was generally lower than in the upwind lobe. This came from the fact that the post-shock wind upwind of the vortex ring had blown away most of the upwind AGN plasma that was deposited at early times, leaving only relatively fresh, unmixed AGN plasma. However, all of the downwind AGN plasma had been retained and become entrained with substantial ICM plasma in response to the penetration of the ICM-driven shock. The jets themselves, on both sides, actually remained essentially fresh, unmixed AGN-injected plasma.

This explanation is reinforced by the $\alpha_{150/600}$ distributions on the right in Figure 11. Although at $t = 119$ Myr, both RG lobes exhibit spectra similar to the injected, $\alpha = 0.6$, virtually

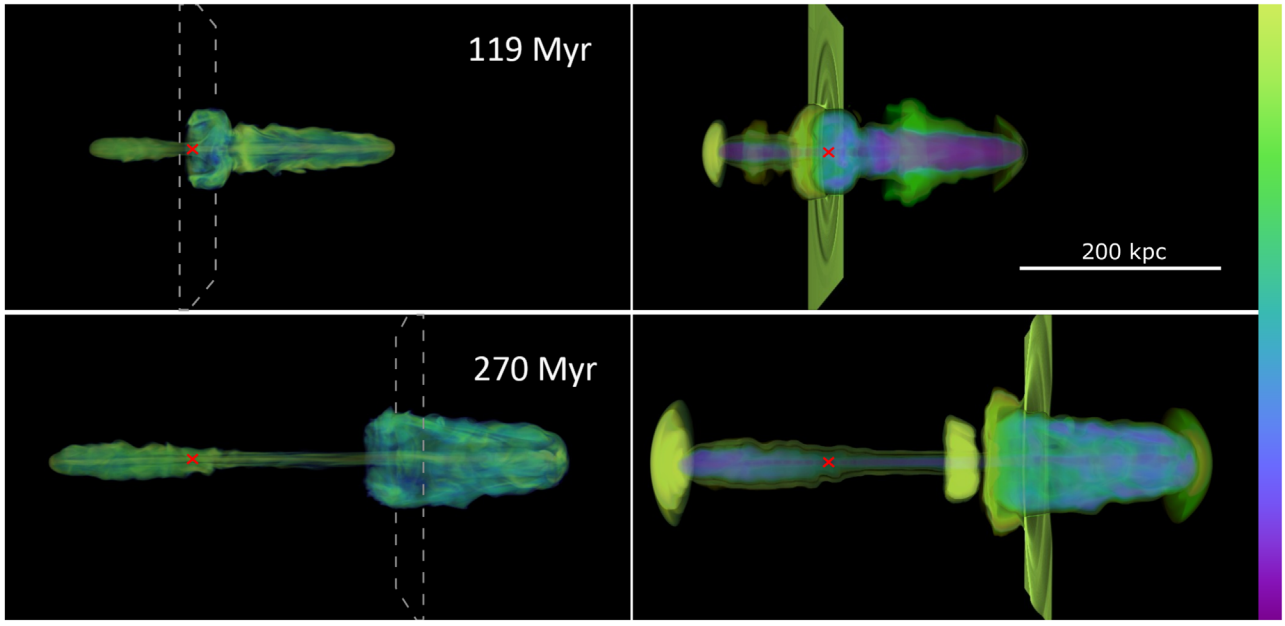

Figure 9. Volume renderings of the J3S2 simulation at two times following shock impact. Orientations are the same as in Figure 3. Left: jet mass fraction (>30% visible). Right: log mass density spanning 3 decades in ρ, with key dynamical features highlighted. The ICM shock is visible at both times. The AGN location is marked by a red cross. As in Figure 3, the location of the external ICM shock is outlined in dashed gray on the left and directly observable in the density on the right.

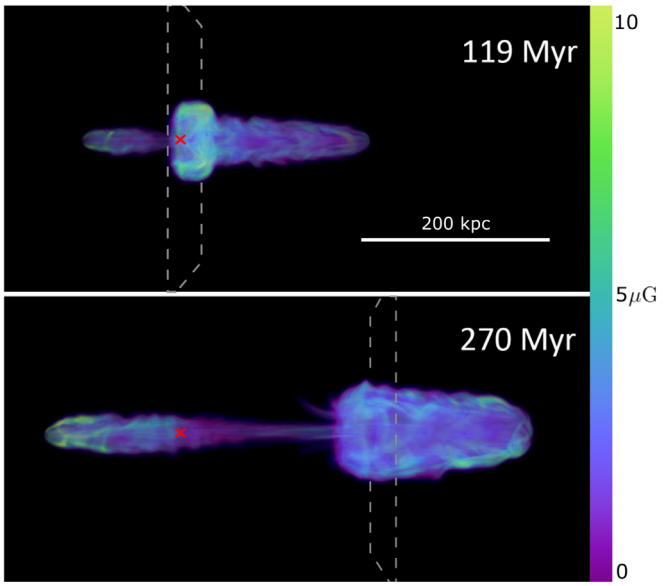

Figure 10. Volume rendering of the magnetic field intensity in the J3S2 simulation at the times in Figure 9. The AGN is marked with a red cross. As in previous figures, the location of the external ICM shock is outlined in dashed gray.

all of the high surface brightness regions in the upwind lobe are flatter (so dominated by younger CRe) than any portion of the downwind lobe except its very tip, where the downwind jet was actively depositing fresh AGN CRe within ~10 Myr of its injection at the AGN. The spectrum of the nascent vortex ring is notably steeper, with $\alpha_{150/600} \gtrsim 1$, but, since this region also contained the strongest magnetic fields at this time, it was radio-bright. At the later time, $t = 270$ Myr, $\alpha_{150/600} \gtrsim 1.2$ everywhere on the downwind side except for the jet itself and small regions of freshly deposited CRe in the head of the lobe. This reflects the fact that the emitting CRe population in the lobe on this side had accumulated for almost 300 Myr, so it was significantly aged. Recall the radiative cooling times of the radio-visible CRe, $\tau_{\rm rad} \lesssim 100$ Myr. Since the magnetic fields in the downwind lobe were not generally stronger than those in the upwind lobe, the aged, steeper-spectrum downwind CRe population led to reduced synchrotron surface brightness along with steeper synchrotron spectra.

The properties just outlined come together to account for the source-integrated spectrum of J3S2 illustrated at multiple times in Figure 12. Before $t \sim 100$ Myr, the integrated fluxes and spectra are rather similar to those in J3S4a and show only modest evidence of aging, reflecting the minor differences in the RG evolutions to that point and steady contributions of fresh CRe to dominant emission regions. At later times, although the integrated spectra of both objects steepen and are similar at low frequencies, the spectra of J3S4a are significantly steeper at high frequencies, reflecting the importance to J3S4a of the isolated vortex ring with its aging CRe population.

4.3. Simulation J3S22: $\theta_{\rm j} = 15°$, $M_{\rm ji} = 3.5$, $M_{\rm si} = 2.25$

Both of the J3S4a and J3S2 simulations included exact alignment between the AGN jet axis and the ICM shock normal ($\theta_j = 0$). The simulation J3S22, with $\theta_j = 15°$, breaks the axisymmetry of those aligned interactions but still develops behaviors that are similar in many ways to the aligned interactions. Here we point out some obvious differences due to the symmetry breaking, but we defer to B. J. O'Neill et al. 2019a, in preparation, the analysis of the more general problem of jets interacting with crosswinds at an arbitrary angle, θ_j, to make twin-tailed structures.

Except for alignment, the jet properties in J3S22 were exactly the same as those in J3S4a and J3S2. The incident shock was given a Mach number, $M_{si} = 2.25$, which, from Equations (11) and (12) for aligned jet–shock encounters, we estimated, after adjusting for the alignment, should just stop forward progress of the upwind jet (see also Figure 2). In that regard, J3S4a is a closer analogy to J3S22 than J3S2, in which the upwind jet was not reversed. On the other hand, the high

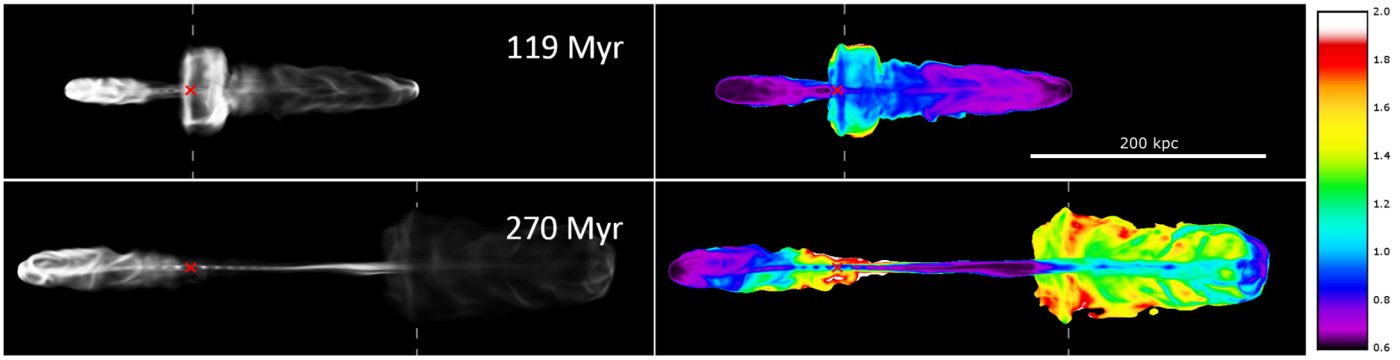

Figure 11. Synchrotron images from J3S2 at the times in Figure 9. Resolution is 0.5 kpc. The AGN jet axis and shock normal are in the plane of the sky. Left: 150 MHz intensity, with the brightest pixel in each image approximately the highest intensity at a given time excluding the jet launch cylinder. Right: 150/600 MHz spectral index for regions above 0.125% of the peak intensity at 150 MHz. The spectral index scale is on the far right. At launch, the jet spectral index was $\alpha = 0.6$. The AGN is marked with a red cross. The location of the external ICM shock is denoted by a dashed gray line.

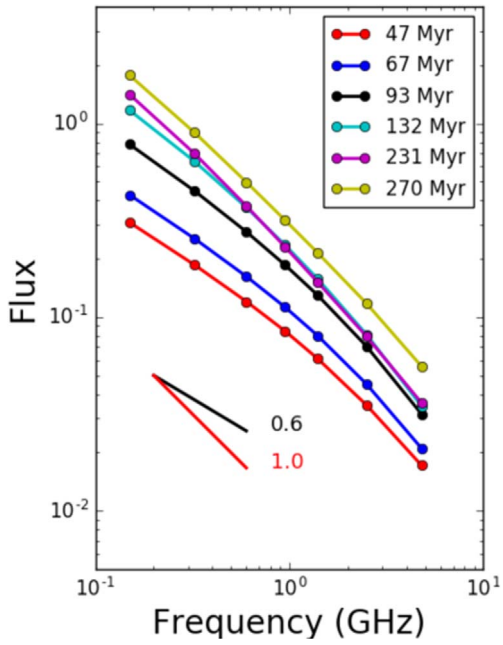

Figure 12. Evolution of the J3S2 integrated synchrotron spectrum.

pressure in the post-shock wind in J3S4a led the jet flows to become subsonic, while Equation (13) suggested that the jets in J3S22 would remain supersonic. That expectation was confirmed by the simulations.

Otherwise, we anticipated two principal differences between J3S4a and J3S22, both coming from the symmetry break. First, we expected (and confirmed) that the misalignment of the upwind jet in J3S22 would cause it to be sharply deflected in the downstream direction rather than directly reversed, thus making two close, downwind-facing jets/tails. Second, we expected (and confirmed) that the high-pressure (and high-density) structure developing just upwind of the shock-induced vortex ring would disrupt the downwind jet more by strong deflection than by strong pinching. Beyond the distinctions outlined here, there were no characteristic dynamical patterns in J3S22 that were not qualitatively similar to those found in J3S4a. Consequently, we do not present a detailed analysis of the former.

However, in order to provide some concrete illustration of the consequences of symmetry breaking, we present 150 MHz synchrotron images and associated spectral index maps of J3S22 at $t = 295$ Myr in Figure 13. Two viewing orientations are shown, both with the shock normal in the plane of the sky. In the upper images, the (oblique) jet axis is also in the plane of the sky. This reveals the full physical separation of the two tails, which is generally $\lesssim$30 kpc even several hundred kpc downwind from the AGN. In the images, the upwind (leftward from the cross) jet is aimed upward from horizontal by 15°, while the downwind jet is aimed 15° downward from horizontal. The lower panels differ only in that the plane containing the jet axis has been rotated by 75° around the shock normal (still in the plane of the sky), so that the two tails now appear more nearly overlapping. By this time, the shock itself is well to the right of all of the synchrotron-emitting plasma and out of the image field of view. The vortex ring is well developed, although it is weaker and, because of less magnetic field amplification, not as radio-luminous as it was in J3S4a. As in J3S4a, the downwind jet has been disrupted near the vortex ring. Although the condition derived in Section 4.1 was only marginally satisfied, the pressure imbalance across the jet as it interacted with the vortex flow was still sufficient to deflect the jet substantially, leading to its disruption. One consequence of the break in symmetry can be seen as an apparent bifurcation in the synchrotron emissions from the jet, seen most obviously in the bottom left panel of Figure 13. Ram pressure across the jet exerted by the wind creates shear along the jet boundary that causes the initially toroidal field to become predominantly poloidal. Due to the jet bending, the cylindrical symmetry of the jets is broken, and this poloidal magnetic field forms two distinct filaments on opposite sides of the jet. Since the synchrotron emissivity is especially sensitive to magnetic field strength, the resultant image emphasizes this pattern. A more detailed analysis of this effect is left to B. J. O'Neill et al. 2019b, in preparation.

Qualitatively, the observable structures in J3S22 at $t = 295$ Myr are rather similar to those at $t = 230$ Myr in J3S4a, once we account for differences in wind velocities and their influence on the displacement of the vortex ring over time. The synchrotron spectrum in the vortex ring here is steeper than it was in J3S4a because the weaker magnetic field also means that emissions at a given frequency come from higher-energy CRe. Thus, the spectra are more sensitive to radiative cooling, which again, in this simulation, is dominated by inverse Compton emissions.

We conclude that for moderately misaligned jet–shock interactions, the simple, aligned case analysis provides a

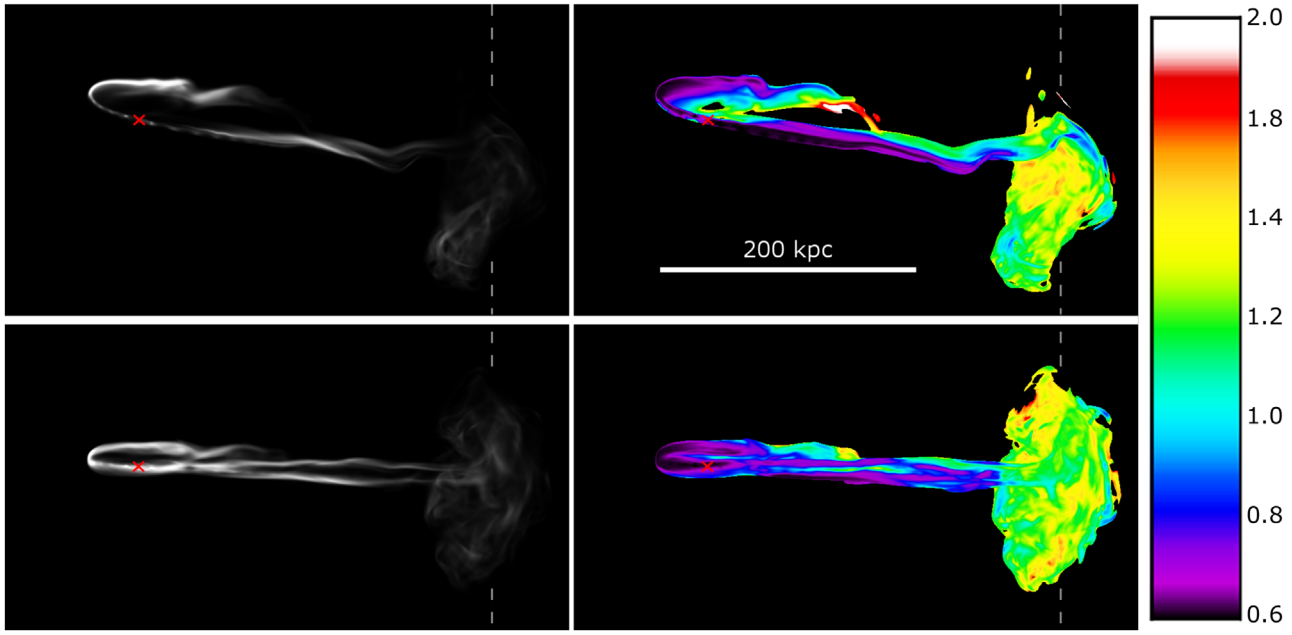

Figure 13. The 150 MHz images (left) and 150/600 MHz spectral index distributions (right) from J3S22 at $t = 295$ Myr. The shock normal is in the plane of the sky. Top: AGN jet axis in the plane of the sky. Bottom: jet–shock normal plane rotated around the shock normal by 75° from the sky. The spectral index color bar is on the far right. The AGN position is marked by a red cross. The location of the external ICM shock is denoted by a dashed gray line.

reasonable dynamical template, although there are some potentially observable consequences of the misalignment. Most significant, of course, the misaligned interaction that reverses the upwind jet really leads to the formation of close tails, rather than a coaxial downwind jet structure. Whether an observer would see the example source in Figure 13 as a single, one-sided tail or twin tails would clearly depend on the projection of the source in the sky, the actual distance to the source, and the effective spatial resolution available to the observer. At $z = 0.2$, the maximum physical separation (∼30 kpc) corresponds roughly to $7\farcs5$. For most projections, the apparent separation would be significantly less than this, of course. Observational separation would likely be challenging but possible (see, e.g., Terni de Gregory et al. 2017).

5. Summary

We have reported a study of the interactions between lobed RGs formed by active supersonic light jets and plane ICM shocks when the RG jet axis and the shock normal are virtually aligned. Our study utilizes 3D MHD simulations designed to test and extend insights coming from simple analytic analyses. The dynamics of those interactions can be decomposed into the impulsive pressure, density, and velocity changes introduced to the RG by the shock discontinuity, followed by the subsequent longer-term interactions between the RG plasma and jets with the post-shock wind.

5.1. Consequences of Shock Passage

As previous studies have emphasized, an ICM shock impacting a low-density RG lobe propagates very rapidly through the lobe, drawing in external ICM plasma and generating strong shear along the lobe perimeter. The most distinctive feature of this shock penetration is the development through boundary shear of a toroidal vortex ring that is carried downwind in the post-shock flow. This vortex can significantly amplify magnetic fields from the RG lobe and, if strong enough, disrupt the RG jets downwind by way of a high-pressure feature that forms along the vortex's toroidal axis.

Our simulations also included a population of relativistic electrons that we used to explore radio synchrotron emissions during the shock–RG encounters. We found that magnetic field amplification, especially coming from field line stretching where vortical motions were strong, could substantially enhance radio emissions in structures produced during the shock encounters. This consequence appears to be especially significant in the large vortex ring structures formed in post-shock flows.

5.2. Consequences of Interaction with a Wind

The predominant consequence of prolonged post-shock wind interaction is the influence of ram pressure on the trajectory of the jets. When, as in this study, the post-shock wind and the jets are aligned, the most direct influence can be characterized in terms of a reduction in the rate at which the upwind jet penetrates into the ICM. For a given set of jet and wind parameters, the resulting behaviors do not depend essentially on the source of the wind but only on its properties with respect to the RG and its host galaxy. The shock applied in this study is only one means to generate the appropriate wind.

A sufficiently strong headwind can reverse the propagation of the upwind jet (or, if they are misaligned, sharply bend that jet into a tail close to the downwind jet/tail). The details of the modifications to jet propagation are sensitive to such things as the ratio of the internal Mach number of the jet and the Mach number of the ICM shock. Thus, the outcomes offer potential metrics of the RG and ICM.

All of these outcomes are rather distinctive and suggest that detailed observations of deformed RGs in clusters could provide valuable insights into both the physics of RG–shock interactions and the character of large-scale ICM dynamical flow patterns.

This work was supported at the University of Minnesota by NSF grant AST1714205 and the Minnesota Supercomputing Institute. C.N. was supported by an NSF Graduate Fellowship under grant 00003920, as well as a travel grant through the School of Physics and Astronomy at the University of Minnesota. We thank numerous colleagues, but especially Larry Rudnick and Avery F. Garon, for encouragement and feedback.

ORCID iDs

Chris Nolting https://orcid.org/0000-0002-0775-6017
T. W. Jones https://orcid.org/0000-0002-9368-4418
Brian J. O'Neill https://orcid.org/0000-0002-1638-8930

References

Begelman, M. C., Rees, M. J., & Blandford, R. D. 1979, Natur, 279, 770
Blumenthal, G. R., & Gould, R. J. 1970, RvMP, 42, 237
Bonafede, A., Intema, H. T., Brüggen, M., et al. 2014, ApJ, 785, 1
Brüggen, M., Bykov, A., Ryu, D., & Röttgering, H. 2012, SSRv, 166, 187
Brunetti, G., Giacintucci, S., Cassano, R., et al. 2008, Natur, 455, 944
Croston, J. H., & Hardcastle, M. J. 2014, MNRAS, 438, 3310
Croston, J. H., Ineson, J., & Hardcastle, M. J. 2018, MNRAS, 476, 1614
Enßlin, T. A., & Brüggen, M. 2002, MNRAS, 331, 1011
Fanaroff, B. L., & Riley, J. M. 1974, MNRAS, 167, 31P
Garon, A. F., Rudnick, L., Wong, O. I., et al. 2019, AJ, 157, 126
Hitomi Collaboration, Aharonian, F., Akamatsu, H., et al. 2016, Natur, 535, 117
Huarte-Espinosa, M., Krause, M., & Alexander, P. 2011, MNRAS, 418, 1621
Jones, T., & Kang, H. 2005, APh, 24, 75
Jones, T. W., Nolting, C., O'Neill, B. J., & Mendygral, P. J. 2017, PhPl, 24, 041402
Jones, T. W., & Owen, F. N. 1979, ApJ, 234, 818
Kravtsov, A. V., & Borgani, S. 2012, ARA&A, 50, 353
Mandal, S., Intema, H. T., Shimwell, T. W., et al. 2019, A&A, 622, A22
Markevitch, M., Gonzalez, A. H., David, L., et al. 2002, ApJL, 567, L27
Mendygral, P. J. 2011, PhD thesis, Univ. of Minnesota
Nagai, D., Vikhlinin, A., & Kravtsov, A. V. 2007, ApJ, 655, 98
O'Neill, S. M., Tregillis, I. L., Jones, T. W., & Ryu, D. 2005, ApJ, 633, 717
Owen, F. N., Rudnick, L., Eilek, J., et al. 2014, ApJ, 794, 24
Padovani, P. 2016, A&ARv, 24, 13
Pfrommer, C., & Jones, T. W. 2011, ApJ, 730, 22
Ranjan, D., Niederhaus, J. H. J., Oakley, J. G., et al. 2008, PhFl, 20, 036101
Rottgering, H., Snellen, I., Miley, G., et al. 1994, ApJ, 436, 654
Ryu, D., Miniati, F., Jones, T. W., & Frank, A. 1998, ApJ, 509, 244
Sarazin, C. L. 1999, ApJ, 520, 529
Schekochihin, A. A., Cowley, S. C., Dorland, W., et al. 2009, ApJS, 182, 310
Shimwell, T. W., Brown, S., Feain, I. J., et al. 2014, MNRAS, 440, 2901
Terni de Gregory, B., Feretti, L., Giovannini, G., et al. 2017, A&A, 608, A58
Tittley, E. R., & Henriksen, M. 2005, ApJ, 618, 227
Tregillis, I. L., Jones, T. W., & Ryu, D. 2001, ApJ, 557, 475
van Weeren, R. J., Andrade-Santos, F., Dawson, W. A., et al. 2017, NatAs, 1, 0005
van Weeren, R. J., Brunetti, G., Brüggen, M., et al. 2016, ApJ, 818, 204
van Weeren, R. J., de Gasperin, F., Akamatsu, H., et al. 2019, SSRv, 215, 16
Voit, G. M. 2005, RvMP, 77, 207
Walker, S., Simionescu, A., Nagai, D., et al. 2019, SSRv, 215, 7
Wilber, A., Brüggen, M., Bonafede, A., et al. 2019, A&A, 622, A25
ZuHone, J. A., & Roediger, E. 2016, JPlPh, 82, 535820301